Convective initiation ahead of the sea-breeze front

Robert G. Fovell

Department of Atmospheric and Oceanic Sciences

University of California, Los Angeles

in press

July, 2004

Corresponding author address: Robert G. Fovell, Department of Atmospheric and Oceanic Sciences, University of California, Los Angeles, 405 Hilgard Ave., Los Angeles, CA, 90095-1565. E-mail: rfovell@ucla.edu.

1

Abstract

In earlier work, a three-dimensional cloud model was used to simulate the interaction between the sea-breeze front (SBF) and front-parallel horizontal convective rolls (HCRs), resulting in the SBF systematically encountering roll updrafts and downdrafts as it progressed inland. Interestingly, deep convection was spawned above an HCR updraft ahead of the SBF as the front approached, well before the inevitable front-roll merger. Ostensibly, both the sea-breeze and roll circulations were required for deep convection to be present in this case at all because convection was entirely absent when either phenomenon was removed.

Further analysis reveals why both circulations were necessary yet not sufficient for the excitation of deep convection in this case. The sea-breeze circulation (SBC) made its upstream (inland) environment more favorable for convection by bringing about persistent if gentle lifting over an extended region stretching well ahead of the SBF. This persistent ascent established a moist and cool tongue of air, manifested by a visible and/or subvisible cloud feature termed the "cloud shelf" emanating ahead of the front. Though this lifting moistened and destabilized the environment, the roll's direct and indirect effects on this moist tongue were also required. The former consisted of a moisture plume lofted by the roll updraft, and the latter, obstacle effect gravity waves generated as the roll drafts penetrated through the top of the boundary layer, into the SBC-associated offshore flow farther aloft. These provided the missing spark which led to rapid growth of cumulus above the roll updraft, drawing first from air located above the boundary layer.

Once established, deep convection above the roll updraft modulated cloudiness above the approaching SBF, at first suppressing it but subsequently assuring its reestablishment and eventual growth into deep convection, again prior to the front-roll merger. This resulted from the influence of gravity waves excited owing to heating and cooling within the roll cloud.

1 Introduction

The initiation of convection along boundary layer convergence lines has been a very active area of research. These convergence features represent and/or are associated with synoptic scale fronts, drylines, thunderstorm outflows (gust fronts), sea-breeze fronts, horizontal convective rolls, topographic features, etc.. Wilson and Schreiber (1986), for example, documented that almost 80% of storms initiated within their Colorado study area occurred in close proximity to radar-detectable convergence features, most commonly associated with thunderstorm outflows. Outflow collisions can provide especially favorable conditions for storm initiation or intensification (e.g., Purdom 1976; Simpson et al. 1980; Tao and Simpson 1984; Droegemeier and Wilhelmson 1985). Wilson et al. (1992) found that storm initiation often occurred where horizontal convective rolls (HCRs) intersected the terrain-induced Denver convergence zone. The role of the sea-breeze circulation (SBC), including the sea-breeze front (SBF), in triggering convection has long been recognized (e.g., Byers and Rodebush 1948; Leopold 1949; Pielke 1974). The interaction of the SBF with river-induced convergence zones (e.g., Zhong et al. 1991; Laird et al. 1995), thunderstorm outflows (e.g., Kingsmill 1995) and HCRs (e.g, Wakimoto and Atkins 1994; Atkins et al. 1995) has been studied observationally, the latter phenomenon having been simulated by Dailey and Fovell (1999) and Rao et al. (1999), for example.

Convective initiation often takes place when two or more features such as fronts and/or rolls collide, merge or otherwise meet. Sometimes, however, the storms crop up prior to any merger. As an example, Nicholls et al. (1991a) mentioned in passing that deep convection could develop in their Florida simulations between the east and west coast SBFs as they came into proximity. Similarly, Fankhauser et al. (1995) examined an outflow-SBF interaction and demonstrated that new convection sprang up in the airmass between the two features,

several minutes prior to their collision. They concluded that a convergence line formed *in situ* within the intermediate airmass as surface heating declined in the late afternoon. Their study focused on events occurring during the Convection and Precipitation/Electrification Experiment (CaPE), conducted in Florida during 1991 (Wakimoto and Lew 1993).

Convective initiation prior to a collision – in this case involving the SBF and an HCR – also occurred in Fovell and Dailey's (2001; "FD01") CaPE-inspired numerical study which employed a high-resolution three-dimensional (3D) cloud model. The initial environmental flow was vertically sheared with the shear vector oriented parallel to an artificially straightened coastline. Small perturbations imposed on the land surface heat flux excited HCRs oriented parallel to the coastline by the early afternoon. The sea-breeze front (SBF) systematically encountered, and merged with, roll updrafts and downdrafts as it progressed inland.

FD01's three simulations consisted of a *sea-breeze only* run resulting from flux perturbation removal, a *roll-only* run lacking the sea subdomain, and a *Control* run which possessed both sea-breeze and roll circulations. The sea-breeze only run generated only shallow clouds situated over the SBF. The roll-only run produced vigorous boundary layer rolls, but these failed to lift air to saturation at any time. Deep convection occurred only in the Control run and that convection was initiated *ahead* of the SBF, ostensibly by a roll and definitely not as a direct consequence of a SBF-roll merger. As in the situation of Fankhauser et al. (1995), the intensity of the convection did increase following the collision but storm initiation took place prior to first contact.

The Control run's most dramatic event is chronicled in Fig. 1. At first, the only cloudiness was associated with the SBF (Fig. 1a). However, the roll cloud that appeared above a nearby roll updraft as the SBF drew closer developed into deep convection prior to SBF-roll contact (Figs. 1b-c). During this period, the roll convection suppressed – at least temporarily – the

SBF cloud (Fig. 1d), resulting in a marked increase in the frontal propagation speed. Yet, the SBF's updraft was itself able to spawn deep convection soon thereafter (Fig. 1e), bringing about a dramatic slowing of the SBF's inland penetration. A brief yet intense downdraft appeared in between the two vertically extensive updrafts, hidden within a single, merged cloud shield.

FD01 examined and explained the initial suppression of the SBF cloud, the propagation speed variations and the transient downdraft's forcing mechanisms. In the present work, we revisit FD01's simulations to discuss these lingering questions:

- Why were both sea-breeze and convective roll circulations required for deep convection to occur at all?

- Why was the roll convection initiated prior to the roll-SBF merger?

- Why was the SBF subsequently able to instigate deep convection itself, after having been negatively influenced by the nearby convective activity?

Section 2 briefly discusses the numerical model employed in this study. The three questions posed above are discussed in Sections 3 and 4. Finally, Section 5 presents a summary.

2   Model

FD01 and Dailey and Fovell (1999) described the idealized numerical model used in this study; please refer to those papers for additional information. Briefly, the model is three-dimensional (3D) with cross-shore, along-coastal and vertical dimensions of 180, 26 and 18

km, respectively. Only one coastline was included, that being straight and oriented north-south with the sea comprising the western 25% (45 km) of the model surface. Horizontal grid spacings were 0.5 and 1 km in the x (cross-shore) and y (along-coastal) directions, respectively; the vertically stretched grid concentrated the highest resolution in the lower troposphere. Only the lateral boundaries were open. Coriolis accelerations and precipitation were excluded from the model solely to simplify the dynamical framework; subgrid scale mixing was handled following Klemp and Wilhelmson (1978). Simulations commenced at sunrise – 0600 LST (local standard time) – with a typical Florida August sounding and a sheared horizontal flow confined to the along-coastal direction. Therefore, all variations in the cross-shore winds were a consequence of the heating-induced circulation(s).

For the Control run, the calculated land surface heat flux was subjected to a $\pm$ 5% normally distributed perturbation in order to encourage 3D motions over land. Boundary layer HCRs appeared throughout the land subdomain in this run shortly before 25800 sec (1310 LST), the time shown in Fig. 1a. Removal of these perturbations yielded the sea-breeze only (SBO) run. Roll-like features eventually appeared in this simulation as well, but rather later in the simulation and were initially confined to the immediate vicinity of the SBF. Detailed intercomparison between the Control and SBO runs is made below, confined to the time interval prior to roll development in the latter. As noted earlier, the roll-only (RO) run resulted when the sea subdomain was removed. Reference will also be made to a "modified SBO" experiment for which a development resembling the Control run's roll convection was artificially provoked in the SBO run.

6

3 Deep convective development in the Control run

It will be shown that the sea-breeze and roll circulations combined synergistically in the Control run, the former making the inland atmosphere more convectively favorable, the latter providing the otherwise missing "spark". Further, analysis suggests the relationship between the roll and the putative roll cloud is more complicated than previously appreciated. We begin by discussing the SBO run, which isolates the SBC modifications that set the stage for convective initiation.

3.1 The sea-breeze circulation in isolation

Figures 2 and 3 document SBC development in the SBO run, culminating at 21600 sec, or local noon. As with Fig. 1 and other figures in this study, these are two-dimensional (2D) fields created by averaging in the along-coastal (north-south) direction. Figure 2's shaded field is perturbation potential temperature (θ'), expressed as a departure from the initial state. In the absence of resolved-scale rolls, the progressive deepening of the neutral boundary layer over land occurred primarily due to subgrid scale turbulence. A sea-breeze front possessing significant ascent (vertical velocity w up to 1.5 m s^{-1}) had already pushed 40 km inland by the final time shown, its relatively rapid progress reflecting the lack of large-scale opposing flow. Above the SBF updraft, vertically propagating gravity waves that were horizontally stationary in the SBF's reference frame are seen. Note that very gentle lower tropospheric ascent (descent) was present ahead (behind) the SBF, having spread well away from the SBF location by local noon, as revealed by the selected contours in Fig. 2c.

Figure 3 presents the ground-relative perturbation horizontal velocity (u') and water vapor

(q'_v) fields averaged in the along-coastal direction. Consistent with classic studies of the SBC (e.g., Walsh 1974; Anthes 1978; Rotunno 1983), the circulation's horizontal component consisted of offshore-directed, middle tropospheric flow overlying winds directed towards land in the lower troposphere. Owing to its long time scales, the SBC's gentle vertical motions eventually engendered substantial environmental alterations, especially to the humidity field. Note in particular the appreciably thick layer of moistened air, centered at roughly 3 km AGL (above ground level), extending far ahead of the SBF. By noon, however, only the air immediately above the SBF had been brought to saturation (see 100% relative humidity contour in Fig. 3c), a situation that will change with further development of the SBC.

The noontime vertical profiles shown in Fig. 4a of w emphasize that the aforementioned gentle lifting was largest at ≈ 2.25 km AGL and possessed a magnitude of 12 cm s^{-1} within 15 km of the front. Figure 4b presents vertical profiles of q'_v as a function of time through the early afternoon at $x = 117$ km, the location where the roll cloud appeared in the Control run. Continued intensification of the SBC, combined with the SBF's approach towards this selected locale, resulted in a marked moistening of the lower to middle troposphere. By 24480 sec, the layer between 3.5 and 4.5 km had become saturated at this location. The Control run's roll cloud appeared in this layer (Fig. 1), and it will be shown (in Fig. 7, below) the cloud signature was already detectable by this particular time.

3.2   Development of roll convection in Control run

The Control and SBO runs commenced with identical conditions, the latter lacking only the small heat flux perturbations employed by the Control run to excite the rolls. Fortuitously, the two simulations retained a considerable amount of similarity for some time, even following the appearance of the rolls in the former. This permits the two to be directly compared, with

8

the *differences between the two runs largely isolating the effect of the rolls upon the SBC*. These difference fields will reveal why both phenomena were required for deep convection, and why the roll cloud was spawned prior to direct roll-SBF contact.

The top two panels of Fig. 5 show Control and SBO run fields of w and cloud water (q_c) at 24480 sec. The cap cloud and gravity wave activity associated with the SBF updraft are evident in both. The waves are stationary in the SBF's reference frame with phase lines tilted from the vertical at an angle α given by (e.g., Holton 1992)

$$\alpha = \cos^{-1}\left[\frac{\hat{\omega}}{N}\right] = \tan^{-1}\left[\frac{L_x}{L_z}\right],\tag{1}$$

where $\hat{\omega}$ and N are the intrinsic and Brunt-Väisällä frequencies, respectively, and the horizontal and vertical wavelengths are L_x and L_z. The phase line sketched on Fig. 5a has $\alpha = 72°$ which, for $N \approx 0.01$ s^{-1}, yields $\hat{\omega} \approx 3.1 \times 10^{-3}$ s^{-1}. By definition, the horizontal phase velocity c_x for this wave is

$$c_x = \frac{\hat{\omega}}{k},$$

where $k = \frac{2\pi}{L_x}$ is the horizontal wavenumber. Since the figure suggests that $L_x \approx 9$ km, c_x is about 4.4 m s^{-1}, equivalent to the SBF propagation speed at this time.

With further SBC development, the aforementioned moistened layer intensified and penetrated farther inland, in both absolute and SBF-relative senses. In contrast to the situation at 21600 sec, in which the only saturated air was found directly above the SBF, a tongue of such air extended almost 30 km ahead of the SBF in both runs by 24480 sec. This created a layer of barely visible or subvisible cloud that will be referred to as the "cloud shelf". Cloud water mixing ratios in the shelf did not exceed 0.05 g kg^{-1} except within the immediate vicinity of the SBF updraft, at least at this time.

Figure 5c presents the Control-SBO difference fields, with positive values denoting larger values associated with the former simulation. Though the SBF position was very nearly the same in these two simulations, the Control run's frontal updraft was somewhat weaker (i.e., $\Delta w < 0$) and its cap cloud contained a little less cloud water ($\Delta q_c < 0$). Naturally, the most obvious distinction is the absence of the boundary layer rolls in the SBO simulation. Yet, the smaller vertical motion discrepancies seen in the 2-6 km tropospheric layer residing directly above the rolls are also of interest. Figure 5's top two panels (along with Fig. 4a) show that $w > 0$ in that layer in both the Control and SBO cases, and thus positive (negative) differences there represented areas where ascent was still present but was relatively stronger (weaker) in the Control run. These roll-associated perturbations were relatively coherent and resided above $z = 3$ km, within the SBC generated offshore flow (Fig. 3). The roll updrafts overshot their neutral buoyancy level (essentially being the mixed layer top) and penetrated into this overlying stable layer, presenting an obstruction to the flow. This resulted in the generation of "obstacle effect" gravity waves (e.g., Mason and Sykes 1982; Clark et al. 1986). The vertical motion discrepancies are manifestations of these waves, the phase lines of which tilt upwind with height, as expected (see also Holton 1992).

Figure 6 qualitatively demonstrates gravity wave generation by the obstacle effect mechanism in a simple 2D model, initialized with environmental conditions resembling those present inland of the SBF in the SBO run at 24480 sec. The horizontal wind was sheared and directed offshore above a 2 km deep neutral layer. Organized vertical motions in that layer were initiated and maintained with a weak streamfunction forcing like that used by Fovell et al. (1992), but repeated in horizontal space and held fixed in time[1]. This forcing generated a series of low-level updrafts and downdrafts that structurally resemble the Control run's HCRs. These pseudo-rolls penetrated slightly into the stable layer above and instigated

---

[1]A subharmonic was included to produce some horizontal variation.

gravity wave activity which manifested tilt angles of about 70°, very close to that seen above the rolls in Fig. 5c, together with essentially identical phasing with respect to the roll drafts below. This tilt angle is determined in part by the strength of the SBC-induced cross-shore flow above the boundary layer, increasing as the wind speed weakens.

Another way in which the boundary layer HCRs influenced the overlying stable layer is by modulating the SBC's background vertical moisture advection. Figure 7 zooms in on the region identified in Fig. 5c and introduces the Control-SBO water vapor difference field, Δq_v. Recall from Fig. 3 that the lower troposphere was being progressively moistened by gentle yet persistent ascent ahead of the SBF (see panel at right). The superposed roll updrafts and downdrafts have served to increase and decrease the absolute humidity of the boundary layer, respectively. These alterations were then spread by resolved scale motions and/or subgrid scale mixing into the stable middle troposphere where they were further influenced by the obstacle effect gravity wave activity and the SBC's offshore flow (also shown at right). These factors were responsible for the Control run's relatively smaller cloud water contents in the cloud shelf above roll downdrafts and within gravity wave downdrafts as well as the augmented cloud water content seen above the roll updrafts. The perturbation that subsequently became the roll convection, representing a 1×10^{-2} g kg^{-1} condensate excess for the Control run, is located at $x = 118$ km, just above a moisture plume lofted by the roll updraft beneath and situated in or very near gravity-wave augmented ascent. Actually, this incipient roll cloud was first identifiable in the same spot about 13 minutes earlier. At that time (not shown), the edge of the cloud shelf had just reached this perturbation, which was but a 5×10^{-5} g kg^{-1} discrepancy.

Though still small at this time, the magnitudes of these differences were growing rapidly. Figure 8 tracks cloud water and vertical velocity differences over the next ≈ 20 min. The roll

cloud became positively buoyant during this time and ascent within the cloud was already ≈ 0.15 m s^{-1} by 25760 sec (Fig. 8d). This increased further to 1 and 3 m s^{-1} after 10 and 20 min, respectively (see Figs. 1b, c).

It may appear from Figs. 1b and 8d that the roll cloud was spawned as the direct result of vertical expansion of the HCR updraft beneath it, carrying lower tropospheric air aloft [as typically happens, for example, in multicell storms; e.g., Fovell and Tan (1998), Fig. 1]. Actually, trajectory analyses suggest the roll cloud was composed almost entirely of *midtropospheric air*, at least at the outset. Figure 9a traces the origins of several air parcels present in the roll cloud during its rapid development phase; none came from the mixed layer (which developed subsequent to the origin time shown anyway). Instead, these three hour backward trajectories reflect the gentle uplift which was taking place upstream (inland) of the SBF, owing to the SBC. The feature we will continue to refer to as the roll cloud did incorporate air from the mixed layer later on (Fig. 9b), but by this time the convection was already well established and vertically extensive.

It is concluded that what we have been calling the "roll cloud" was actually formed *in situ* within the stable layer overlying the HCRs, and we further suggest that it resulted from the combination of the roll's direct (moisture plume) and indirect (via gravity wave) effects on the SBC-induced cloud shelf extending ahead of the SBF. It is conceivable that both roll-associated factors were necessary but not individually sufficient to bring about deep convective development, at least in this case. Supplying a humidity perturbation to the SBO run resembling the moisture plume seen in the Control run (around $x = 120$ km and $z = 2.5$ km in Fig. 7) was by itself not enough to provoke deep convection (not shown). However, as described presently, it was very easy to spawn convection from even a small moisture perturbation placed within the cloud shelf where the incipient roll cloud actually appeared.

Such a moisture perturbation in the Control run could have resulted from the action of the weak, though persistent, obstacle effect gravity wave updrafts. Still, the main point is that the SBC itself made a portion of the environment inland of the SBF convectively favorable, but it took a "spark" provided directly and/or indirectly by the boundary layer rolls in order for deep convection to be realized.

It might be asked why that spark did not come from the nearby SBF which provided a considerable amount of low-level uplift. Yet, recall that the SBO run evinced no deep convection whatsoever, and even in the Control run significant vertical development at the SBF occurred only *after* the roll cloud itself grew into deep convection. It is suggested that the SBF's lifting, though undoubtedly strong and persistent, is generally not very effective. Rotunno et al. (1988; "RKW") examined the problem of lifting over cold pools, and the interaction between by two common sources of horizontal vorticity: that baroclinically generated at the cold pool boundary and that associated with the vertical wind shear. They noted the lifting was deepest and most effective when when the two vorticities were roughly equal and opposing. In contrast, lifted parcels tended to be accelerated laterally more than vertically when the cold pool vorticity was dominant. While in the present situation the baroclinically generated vorticity at the SBF was not very large, the shear – itself a product of the SBC – was also very weak. Further, Fig. 3 shows the shear above 1 km did not oppose the baroclinic vorticity anyway.

Whatever the explanation, there is no doubt that the considerable uplift provided by the SBF was by itself not sufficient. But why then did deep convection finally appear above the SBF in the Control run? In the next section it is argued that the roll convection itself made environmental conditions at the sea-breeze front more thermodynamically favorable, and perhaps more dynamically favorable as well.

4 Redevelopment of SBF convection prior to merger

The development of roll convection exerted a first order impact on the SBF. FD01 examined the SBF cloudiness suppression and the accompanying frontal acceleration that occurred between 26400 and 27600 sec (Figs. 1b-d). The former was attributed to the roll cloud circulation which altered the source and nature of the air arriving at the sea-breeze front; the ensuing reduction in latent heating above the front brought about the latter. Left unexplained was the considerable reintensification and vertical expansion of the SBF updraft, resulting in what we view as a separate deep convective development, that occurred prior to the SBF-HCR merger (Fig. 1e). Below, we interpret both the suppression and the reinvigoration of SBF convection as being induced by the roll cloud, through the agency of gravity waves excited by the cloud's cooling as well as its heating.

Figure 10 documents the result of introducing a moisture perturbation into the SBO run's already saturated midtropospheric cloud shelf. This "modified SBO" (MSBO) experiment isolates the immediate and subsequent effects of a roll cloud-like development on the SBF in a controlled fashion. The elliptically shaped perturbation employed here had vertical and horizontal radii of 1 and 2 km, respectively, and was centered at $\approx$ 4 km AGL, the height where the Control run's incipient roll cloud first appeared (Fig. 7). The moisture augmentation was purposely made larger in size and magnitude than that which existed in the Control run at this time and the new cloud quickly escalated into deep convection, possessing a fairly vigorous midtropospheric updraft flanked by downdrafts within five minutes (Fig. 10a). As in the Control run, the SBF cloudiness began dissipating soon thereafter. The analysis below makes use of MSBO-SBO difference fields, again designated by the symbol Δ.

The immediate environmental response to this suddenly introduced source of latent heating took the form of deep tropospheric subsidence, carried away in both directions by gravity waves (e.g., Nicholls et al., 1991b; "NPC"). That response can be seen in both Fig. 10a's w field and Fig. 10b's potential temperature difference ($\Delta\theta$) distribution. Indeed, the latter shows that the seaward-propagating subsidence wave was clearly responsible for the SBF cloudiness suppression that ensued in both the Control and MSBO cases (Figs. 1d and 10b). The encounter of the subsidence with the SBF cloud is especially obvious; note the compression warming was neutralized above the front where the SBF cloud was forced to evaporate (i.e., where $\Delta q_c < 0$), breaking the relative symmetry of the field. The SBF propagation speed also increased around this time, consistent with the sequence of events in the Control run.

However, as in the Control experiment, this SBF updraft and cloudiness suppression was short-lived and soon gave way to reinvigoration. This reintensification is believed to be largely the result of a second environmental adjustment, this having been provoked by the development of persistent localized cooling beneath the new cloud. The contoured field in Fig. 10a depicts the combination of vertical potential temperature advection and latent heating/cooling terms called TVPT by Fovell and Tan (1988). In updraft areas, TVPT < 0 indicates locations where adiabatic cooling exceeded latent heat release (if any). Negative TVPT is seen in the lower portion of the new cloud's updraft, at $z = 3$ km. A small region of locally cooler air did indeed appear beneath this cloud soon thereafter (Fig. 10b).

It has been shown (e.g., NPC; Mapes 1993; Shige and Satomura 2000; Fovell 2002, etc.) that an elevated source of cooling, whether diabatic or adiabatic in origin, can also provoke gravity waves, these being characterized by lower tropospheric ascent. Since the cooling source was much shallower, the waves it excited had a shorter vertical wavelength and thus

a slower propagation speed than the primary subsidence wave. Therefore, this secondary wave travelled through the subsidence wave's wake, its ascent acting to mitigate the effects of its predecessor. Part of this secondary response is highlighted on Fig. 10c, its western and eastern leading edges represented by the lower tropospheric $w=0$ phase lines located at $x = 109$ and 124 km, respectively. Indeed, despite the complicating influence of the SBC's lower tropospheric flow in this case, the vertical velocity field in and around the upstream cloud in Fig. 10c is strongly reminiscent of Shige and Satomura's (2000) Fig. 5.

Figure 10's final panel captures the secondary wave's lower tropospheric ascent as it spread upwind towards the SBF. As shown by the figure's Δq_v fields, this lifting worked to moisten the upper boundary layer and midtroposphere, starting with the eradication of the drying caused by the previous subsidence wave. This is why the larger positive Δq_v values lagged behind the secondary wave's leading edge. That is also revealed by Fig. 11, which presents a time series of Δw and Δq_v at $x = 113$ km, a location residing between the new cloud and the SBF. These data were taken at 2.8 km elevation, the level at which the secondary wave's lifting was strongest, and thus capture the timing, but not the full magnitude, of the deep initial subsidence which had its largest signal farther aloft.

Thus, the environment in between the SBF and the "roll cloud" was in the process of being altered yet again, this time apparently bringing about conditions favoring redevelopment of the SBF cloudiness. It is possible there was a dynamic contribution as well, more likely due to the gravity wave induced alterations in the vertical wind shear than the concomitant frontal acceleration. Figure 12 presents vertical profiles of Δu, representing the horizontal velocity change responding to the artifically induced convection, again for the intervening location of $x = 113$ km. Recall from the preceding subsection that the low-to-midtropospheric vertical shear was not optimal in the RKW sense for effective SBF lifting prior to the development

of the artifically induced cloud, and the times designated 2 and 3 show the initial subsidence wave did not ameliorate that situation. The passage of the secondary gravity wave (times 4-6), however, established a fairly substantial positive shear vorticity, opposite in sign to the baroclinically generated vorticity, at least above 2 km. While the shear in contact with the cold pool (here, marine flow) is more important in determining the effectiveness of the frontal lifting (e.g., RKW), the shear farther aloft is also influential. This was demonstrated in squall lines by Fovell and Dailey (1995).

As in the Control run (see Figs. 1d-e), redevelopment ensued as the secondary gravity wave reached the SBF. The degree of SBF cloud regrowth is ostensibly controlled by the strength of the environmental adjustment as well as the distance from the SBF and the upstream cloud's origin. The latter influences the amount of time between the arrival of the invigorating secondary wave and when the updraft cloud itself gets too close.

5   Discussion and summary

We now summarize with the aid of the schematic presented in Figure 13, which depicts a vertical plane straddling the coastline. The top panel sketches the principal consequences of the sea-breeze circulation (SBC), itself a response to daytime land/sea heating contrasts. A tongue of moistened air extends inland ahead of the sea-breeze front (SBF), the leading edge of the marine air that is typically topped by shallow cloudiness. The moistening occurs owing to the SBC's gentle yet persistent lifting over the land. Closer to the SBF itself, the tongue's air may be saturated, resulting in a layer of visible or subvisible cloud termed the "cloud shelf" herein. In advance of the SBF, onshore (offshore) flow is induced within (above) the mixed layer that forms owing to the resolved and subgrid scale mixing generated

17

as the ground surface is heated.

In a vertically sheared flow, variations in surface heating can organize the resolved scale eddies into horizontal convective rolls (HCRs), typically aligned with the low-level shear vector. In this case, the initial shear flow was unidirectional and oriented along the coastline (into the page), so the SBF was systematically encountering roll updrafts and downdrafts aligned parallel to it as it moved inland. One such roll updraft is shown in Fig. 13b. The draft protrudes into the stable layer above, presenting an obstacle within the offshore branch of the SBC's horizontal airflow. This results in obstacle effect gravity waves that lean up-wind with height; these waves can cause spatial variations of humidity within the tongue of moistened air and the cloud shelf. Variations also result owing to vertical moisture advection accomplished by the rolls. Local regions of of higher absolute and relative humidity are found above the roll updrafts, where they extend above the mixed layer. This is designated as the "moisture plume" on Fig. 13b.

These direct (moisture plume) and indirect (obstacle generated gravity waves) effects of the HCRs appeared to combine synergistically to establish the roll cloud (Fig. 13c) ahead of the advancing SBF in the Control run. In particular, that cloud was initiated as the leading edge of the cloud shelf passed above an especially intense HCR updraft. The roll cloud, however, was initially composed of air originating above the mixed layer, and so was generated *in situ* within the cloud shelf. As the cloud developed into deep convection, however, its circulation started drawing air up from the boundary layer.

As the roll cloud developed, it exerted a dramatic impact on its surrounding environment, including the cloud perched above the oncoming SBF. This impact was carried by another kind of gravity wave, responding to thermal forcing within the intensifying convection. The initial response to the onset of heating within the roll cloud was deep subsidence which

caused drying, particularly in the middle troposphere. That drying represented the agent of initial SBF cloud suppression. Relieved of latent heating above it, the cross-frontal pressure difference (not shown on figure) increased, accelerating the SBF inland.

However, prior to the inevitable SBF-roll merger, the SBF cloud subsequently not only reappeared but also developed into deep convection itself, something that did not occur in simulations in which the rolls (and especially their consequences) were excluded. That appeared to be less due to enhanced SBF convergence than to a secondary thermally forced gravity wave, this one responding to localized, shallow adiabatic and/or diabatic cooling beneath the developing roll cloud. As a consequence, this gravity wave had a smaller vertical wavelength and thus a slower propagation speed. The lower tropospheric portion of this wave consisted of ascent, resulting in moistening and cooling that mitigated the effects of the previous subsidence wave, at least in the lowest several kilometers. This lifting spread upwind towards the SBF, representing the agent of subsequent SBF cloud reintensification.

References

Anthes, R. A., 1978: The height of the planetary boundary layer and the production of circulation in a sea breeze model. *J. Atmos. Sci.,* **35**, 1231-1239.

Atkins, N. T., R. M. Wakimoto, and T. M. Weckwerth, 1995: Observations of the Sea-Breeze Front during CaPE. Part II: Dual-Doppler and Aircraft Analysis. *Mon. Wea. Rev.,* **123**, 944-968.

Byers, H. R., and H. R. Rodebush, 1948: Causes of thunderstorms of the Florida peninsula. *J. Atmos. Sci.,* bf 5, 275-280.

Clark, T. E., T. Hauf, and J. P. Kuettner, 1986: Convectively forced internal gravity waves: Results from two-dimensional experiments. *Quart. J. Roy. Meteor. Soc.,* **112**, 899-926.

Dailey, P. S., and R. G. Fovell, 1999: Numerical simulation of the interaction between the sea-breeze front and horizontal convective rolls. Part I: Offshore ambient flow. *Mon. Wea. Rev.,* **127**, 858-878.

Droegemeier, K. K., and R. B. Wilhelmson, 1985: Three-dimensional numerical modeling of convection produced by interacting thunderstorm outflows. Part I: Control simulation and low-level moisture variations. *J. Atmos. Sci.,* **42**, 2381-2403.

Fankhauser, J. C., N. A. Crook, J. Tuttle, L. J. Miller, and C. G. Wade, 1995: Initiation of deep convection along boundary layer convergence lines in a semitropical environment. *Mon. Wea. Rev.,* **123**, 291-314.

Fovell, R. G., 2002: Upstream influence of numerically simulated squall-line storms. *Quart.*

J. Roy. Meteor. Soc., **128**, 893-912.

——, and P. S. Dailey, 1995: The temporal behavior of numerically simulated multicell-type storms. Part I: Modes of behavior. *J. Atmos. Sci.,* **52**, 2073-2095.

——, and ——, 2001: Numerical simulation of the interaction between the sea-breeze front and horizontal convective rolls. Part II: Alongshore ambient flow. *Mon. Wea. Rev.,* **129**, 2057-2072.

——, and P.-H. Tan, 1998: The temporal behavior of numerically simulated multicell-type storms. Part II: The convective cell life cycle and cell regeneration. *Mon. Wea. Rev.,* **126**, 551-577.

Fovell, R., D. Durran, and J. R. Holton, 1992: Numerical simulations of convectively generated stratospheric gravity waves. *J. Atmos. Sci.,* **49**, 1427-1442.

Holton, J. R., 1992: *An Introduction to Dynamic Meteorology*, Third Edition. Academic Press, San Diego, pp. 511.

Kingsmill, D. E., 1995: Convection initiation associated with a sea-breeze front, a gust front, and their collision. *Mon. Wea. Rev.,* **123**, 2913-2933.

Klemp, J. B., and R. B. Wilhelmson, 1978: The simulation of three-dimensional convective storm dynamics. *J. Atmos. Sci.,* **35**, 1070-1096.

Laird, N. F., D. A. R. Kristovich, R. M. Rauber, H. T. Ochs, and L. J. Miller, 1995: The Cape Canaveral sea and river breezes: Kine-matic structure and convective initiation. *Mon. Wea. Rev.,* **123**, 2942-2956.

Leopold, L. B., 1949: The interaction of trade wind and sea breeze, Hawaii. *J. Meteor.*, **6**, 312-320.

Mapes,B.E., 1993: Gregarious tropical convection. *J. Atmos. Sci.,* **50**, 2026-2037.

Mason, P. J., and R. I. Sykes, 1982: A two-dimensional numerical study of horizontal roll vortices in an inversion capped planetary boundary layer. *Quart. J. Roy. Meteor. Soc.,* **108**, 801-823.

Nicholls, M. E., R. A. Pielke, and W. R. Cotton, 1991a: A two-dimensional numerical investigation of the interaction between sea breezes and deep convection over the Florida peninsula. *Mon. Wea. Rev.,* **119**, 298-323.

——, ——, and ——, 1991b: Thermally forced gravity waves in an atmosphere at rest. *J. Atmos. Sci.,* **48**, 1869-1884.

Pielke, R. A., 1974: A three-dimensional numerical model of the sea breezes over south Florida. *Mon. Wea. Rev.,* **102**, 115-139.

Purdom, J. F. W., 1982: Subjective interpretation of geostationary satellite data for now-casting. In *Nowcasting*, Keith Browning, Ed., Academic Press, 149-156.

Rao, P. A., H. E. Fuelberg, and K. K. Droegmeier, 1999: High-resolution modeling of the Cape Canaveral area land-water circulations and associated features. *Mon. Wea. Rev.,* **127**, 1808-1821.

Rotunno, R., 1983: On the linear theory of the land and sea breeze. *J. Atmos. Sci.,* **40**, 1999-2009.

——, J. B. Klemp, and M. L. Weisman, 1988: A theory for strong, long lived squall lines. *J. Atmos. Sci.,* **45**, 463-485.

Shige, S., and T. Satomura, 2000: The gravity wave response in the troposphere around deep convection. *J. Meteor. Soc. Japan,* **78**, 789-801.

Simpson, J., N. E. Westcott, R. J. Clerman, and R. A. Pielke, 1980: On cumulus mergers. *Arch. Meteor. Geophys. Bioklim.*, Ser. A., **29**, 1-40.

Tao, W.-K., and J. Simpson, 1984: Cloud interactions and merging: Numerical simulations. *J. Atmos. Sci.,* **41**, 2901-2917.

Wakimoto, R. M., and J. K. Lew, 1993: Observations of a Florida waterspout during CaPE. *Wea. Forecasting,* **8**, 412-423.

——, and N. T. Atkins, 1994: Observations of the sea-breeze front during CaPE. Part I: Single-doppler, satellite and cloud photogrammetry analysis. *Mon. Wea. Rev.,* **122**, 1092-1113.

Walsh, J. E., 1974: Sea breeze theory and applications. *J. Atmos. Sci.,* **31**, 2012-2026.

Wilson, J. W., and W. E. Schreiber, 1986: Initiation of concective storms at radar-observed boundary-layer convergence lines. *Mon. Wea. Rev.,* **114**, 2516-2536.

——, G. B. Foote, N. A. Crook, J. C. Fankhauser, C. G. Wade, J. D. Tuttle, C. K. Mueller, and S. K. Krueger, 1992: The role of boundary-layer convergence zones and horizontal rolls in the initiation of thunderstorms: A case study. *Mon. Wea. Rev.,* **120**, 1785-1815.

Zhong, S., J. M. Leone, Jr., and E. S. Takle, 1991: Interaction of the sea breeze with a river

breeze in an area of complex coastal heating. *Bound.-Layer Meteor.*, **56**, 101-139.

Figure captions

Figure 1 - Control run fields of vertical velocity (w, 0.5 m s^{-1} thin contours) and cloud water mixing ratio (q_c, 0.5 g kg^{-1} thick contours), averaged in the along-coastal direction. The 5 m s^{-1} contour of ground-relative cross-shore horizontal velocity, a proxy for the marine air boundary, is superposed; its leading edge is the sea-breeze front (SBF). Contours for negative values dashed; only a portion of the domain is shown. Times shown relative to sunrise (0600 local standard time).

Figure 2 - Sea-breeze only (SBO) run along-coastal averaged fields of perturbation potential temperature (θ', shaded) and vertical velocity (w, 0.5 m s^{-1} contours). Perturbations are relative to the initial state. Contours for negative values dashed. Selected contours of $w = \pm\, 0.05$ m s^{-1} are superposed.

Figure 3 - SBO run fields of perturbation vapor mixing ratio (q_v', shaded) and horizontal (cross-shore) velocity (u, 2 m s^{-1} contours). Contours for negative values dashed. Thick white contour encloses saturated region.

Figure 4 - Vertical profiles of along-coastal averaged quantities from the SBO run: (a) vertical velocity w at 21600 sec for specified distances ahead of the SBF; (b) perturbation vapor q_v' profiles at various times for a selected location ($x = 117$ km; see Figs. 2 and 3). Thick grey lines mark height levels where saturation has been achieved.

Figure 5 - Control, SBO and Control-SBO difference fields at 24480 sec. Panels (a) and (b) show vertical velocity w (shaded and contoured) and cloud water q_c (0.5 g kg^{-1} thick contours) with saturated region identified. Panel (c) depicts vertical velocity and cloud water difference fields Δw and Δq_c. Contour interval for Δq_c is 0.1 g kg^{-1}. Contours for negative values dashed. Figure 7's subdomain is delineated.

Figure 6 - Pseudo-roll simulation employing a maintained streamfunction field with weak forcing to generate roll-like circulations, showing vertical velocity w (shaded/contoured) and perturbation potential temperature θ' (0.005 K contours). Contours for negative values dashed. Profiles of u and θ at right resembles those present inland of the SBF in the early afternoon. (Vertical shear within the mixed layer has been neglected for simplicity.)

Figure 7 - Control-SBO difference fields at 24480 sec. Shown are: vertical velocity Δw (shaded), water vapor mixing ratio ($\Delta q'_v$, 0.1 g kg^{-1} thin black contours) and cloud water mixing ratio (δq_c, 0.01 g kg^{-1} thick grey contours) difference fields. Contours for negative values dashed. Saturated region from the SBO run is marked. Vertical profiles of u and w from the SBO run at a designated location reveals the background field upon which the Control run's rolls are superposed.

Figure 8 - Control-SBO vertical velocity (Δw, shaded/contoured) and cloud water (Δq_c) difference fields. Δq_c contours selected for inclusion are the 0.01, 0.05, 0.09, 0.13 and 0.17 g kg^{-1} isolines, in addition to the -0.0001 and -0.025 g kg^{-1} values. Contours for negative values dashed.

Figure 9 - Control run w (shaded/contoured) and q_c (contoured) fields with backward trajectories started at time shown: (a) fields at 25440 with q_c contour interval of 0.05 g kg^{-1}; (b) fields at 26400 sec with q_c contour interval 0.2 g kg^{-1}. Contours for negative values dashed. Please note cloud water contour intervals are not the same, and differ from that employed in Fig. 1.

Figure 10 - Fields from the modified SBO (MSBO) run along with MSBO-SBO differences, depicting: (a) vertical velocity w (shaded/contoured), 0.5 g kg^{-1} cloud water outline (in white) and TVPT (0.02 K s^{-1} contours) at 24800 sec, 5 min after introduction of moisture perturbation in SBO run's cloud shelf; (b) MSBO-SBO potential temperature difference field ($\Delta\theta$, shaded/contoured) at 25320 sec with $\pm$ 0.15 g kg^{-1} cloud water (Δq_c,) difference contours (in white) superposed; (c) MSBO w field (0.5 m s^{-1} contours) at 25320 sec with $\Delta\theta$ silhouette for reference; and (d) w (0.5 m s^{-1} contours) and water vapor difference (Δq_v, shaded/contoured) fields at 25640 sec. Contours for negative values dashed. In (b), position of the MSBO SBF updraft shown by the 0.5 m s^{-1} w contour.

Figure 11 - Time series of MSBO-SBO vertical velocity and vapor mixing ratio difference fields, commencing at time of cloud shelf perturbation introduction in the latter, for the location $x = 113$ km and $z = 2.8$ km (refer to Fig. 10).

Figure 12 - Vertical profiles of MSBO-SBO horizontal velocity difference (Δu) at the location $x = 113$ km (refer to Fig. 10) for a variety of times following cloud shelf perturbation introduction.

Figure 13 - Schematic depiction of SBC and roll-related influences leading to deep convection ahead of the SBF in the Control run. See text for discussion.
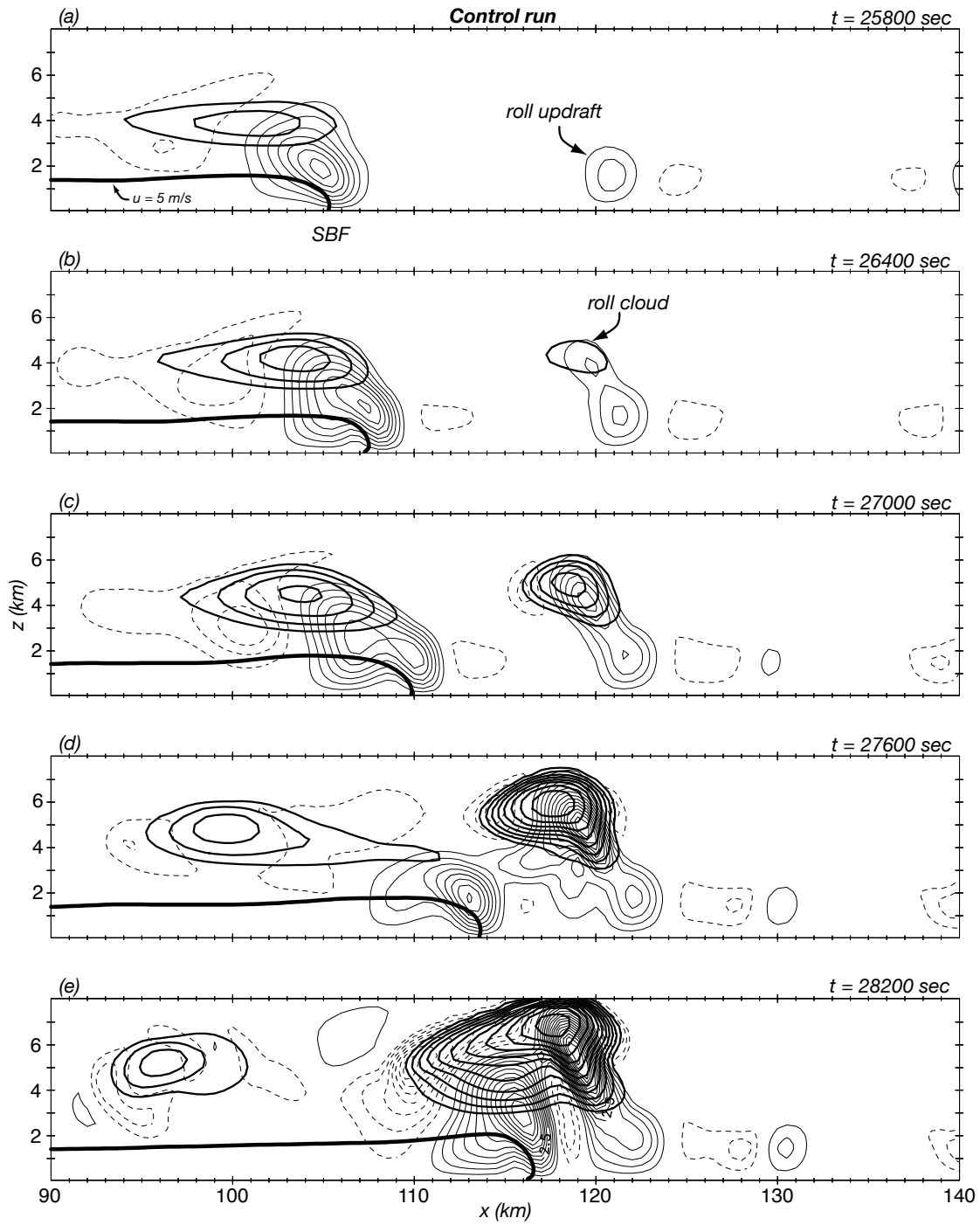
Fig. 1: Control run fields of vertical velocity (w, 0.5 m s^{-1} thin contours) and cloud water mixing ratio (q_c, 0.5 g kg^{-1} thick contours), averaged in the along-coastal direction. The 5 m s^{-1} contour of ground-relative cross-shore horizontal velocity, a proxy for the marine air boundary, is superposed; its leading edge is the sea-breeze front (SBF). Contours for negative values dashed; only a portion of the domain is shown. Times shown relative to sunrise (0600 local standard time).
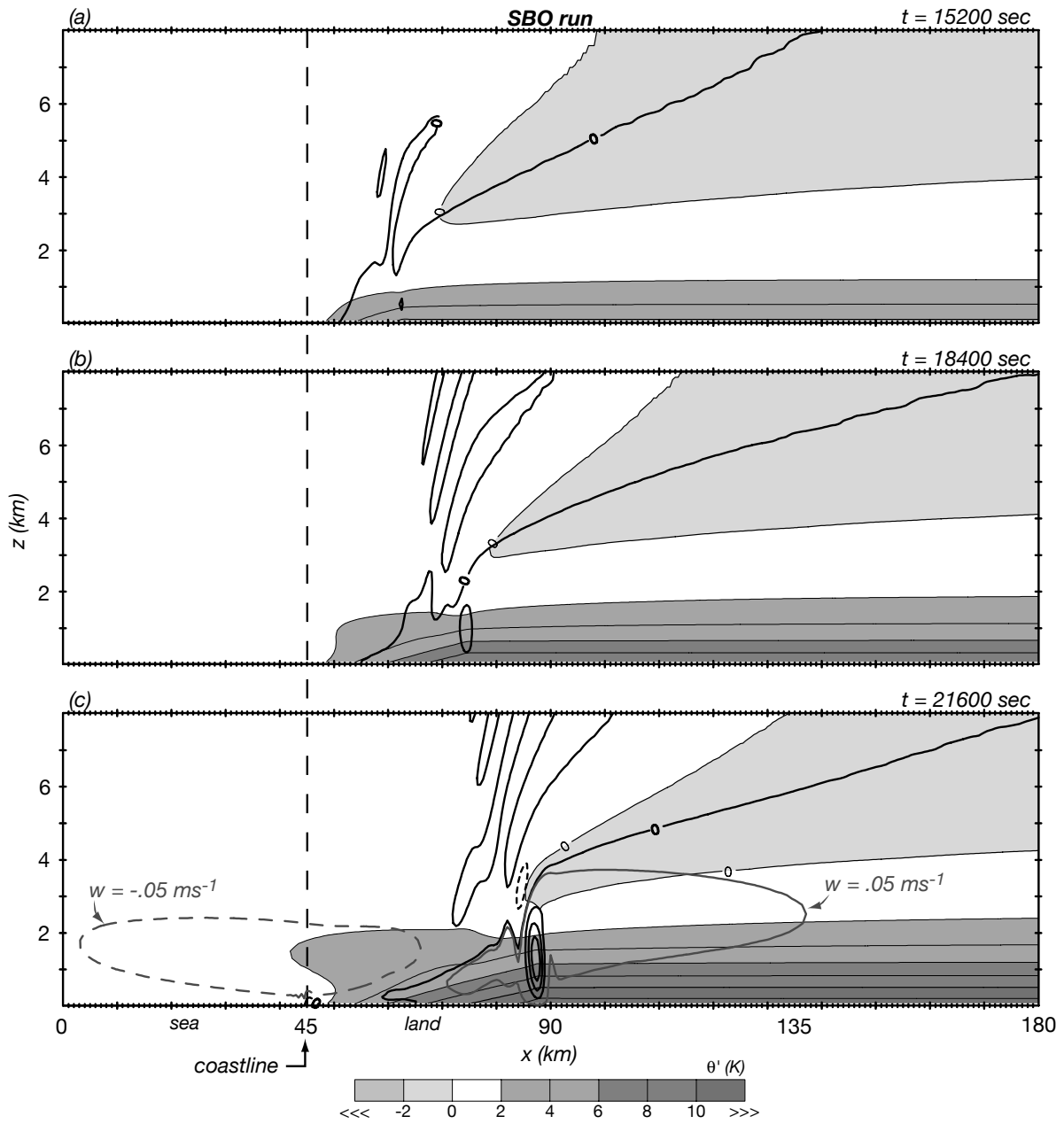
Fig. 2: Sea-breeze only (SBO) run along-coastal averaged fields of perturbation potential temperature (θ', shaded) and vertical velocity (w, $0.5\ \mathrm{m\,s^{-1}}$ contours). Perturbations are relative to the initial state. Contours for negative values dashed. Selected contours of $w = \pm\ 0.05\ \mathrm{m\,s^{-1}}$ are superposed.
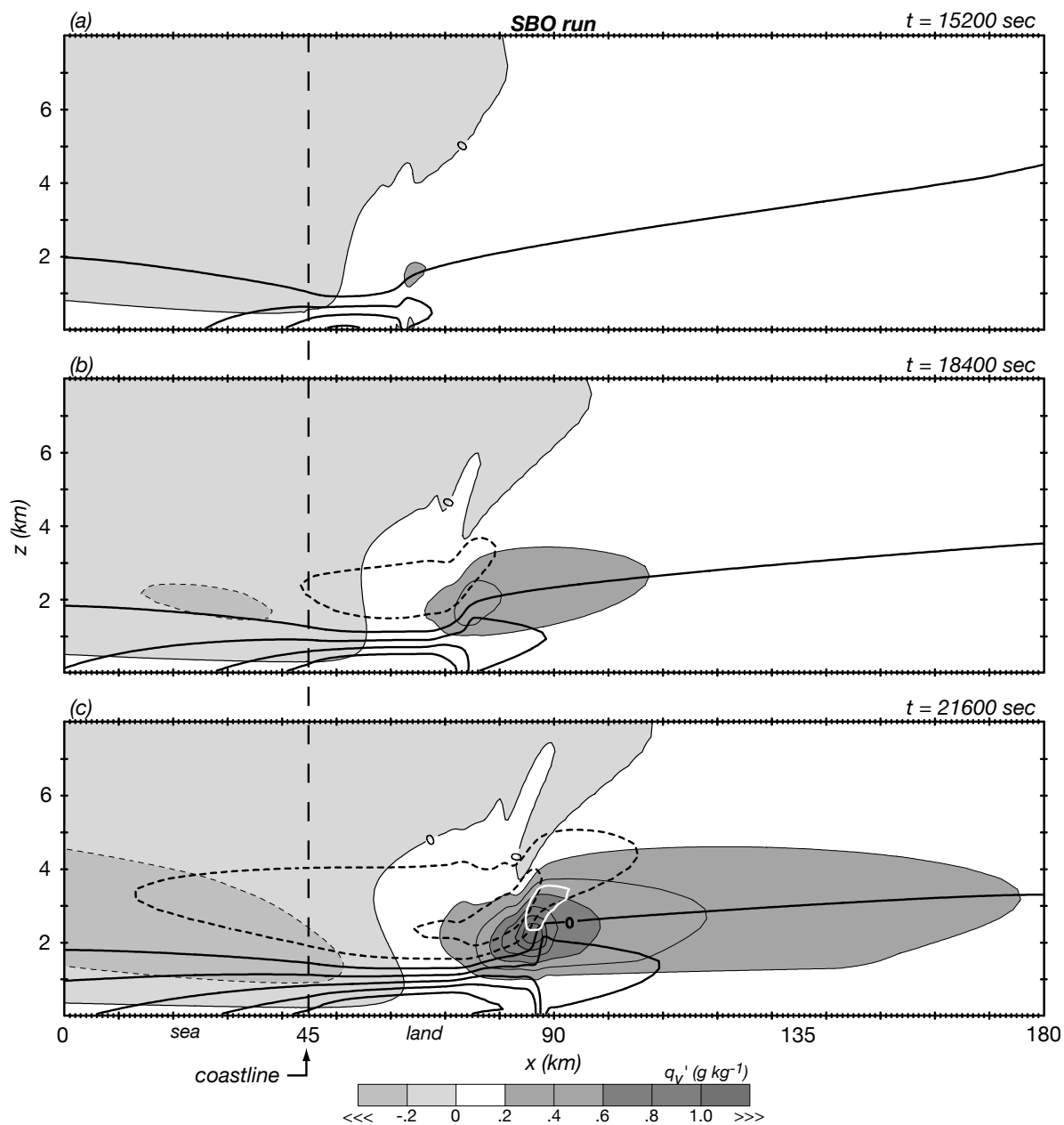
Fig. 3: SBO run fields of perturbation vapor mixing ratio (q'_v, shaded) and horizontal (cross-shore) velocity (u, 2 m s^{-1} contours). Contours for negative values dashed. Thick white contour encloses saturated region.
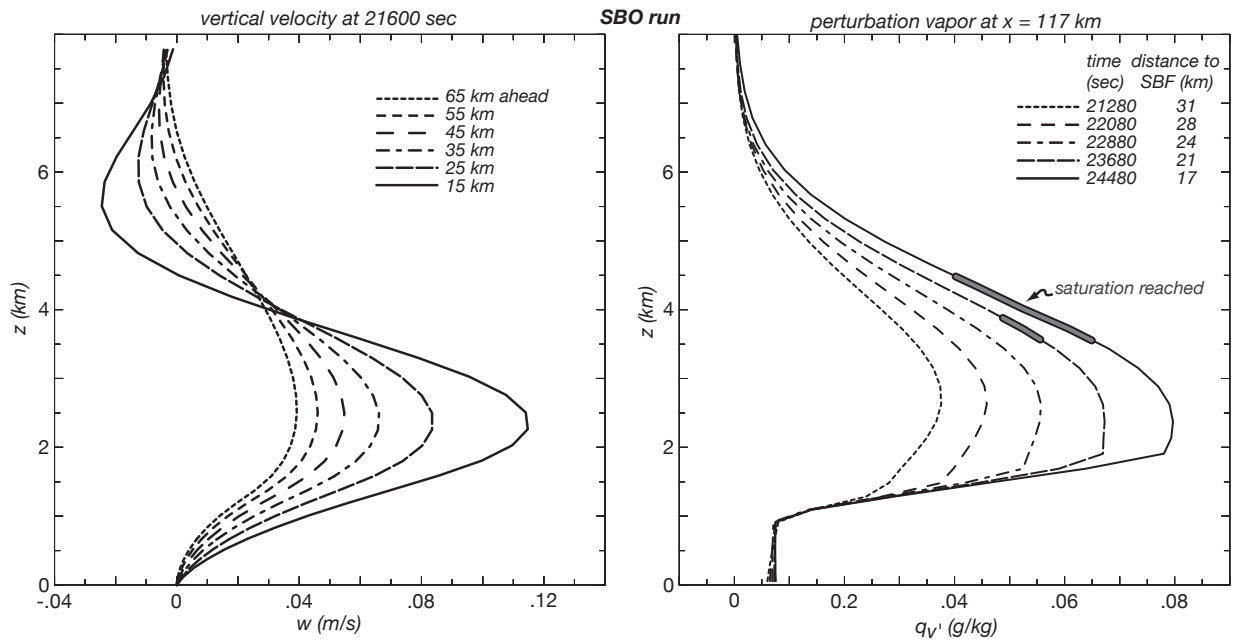
Fig. 4: Vertical profiles of along-coastal averaged quantities from the SBO run: (a) vertical velocity w at 21600 sec for specified distances ahead of the SBF; (b) perturbation vapor q'_v profiles at various times for a selected location ($x = 117$ km; see Figs. 2 and 3). Thick grey lines mark height levels where saturation has been achieved.
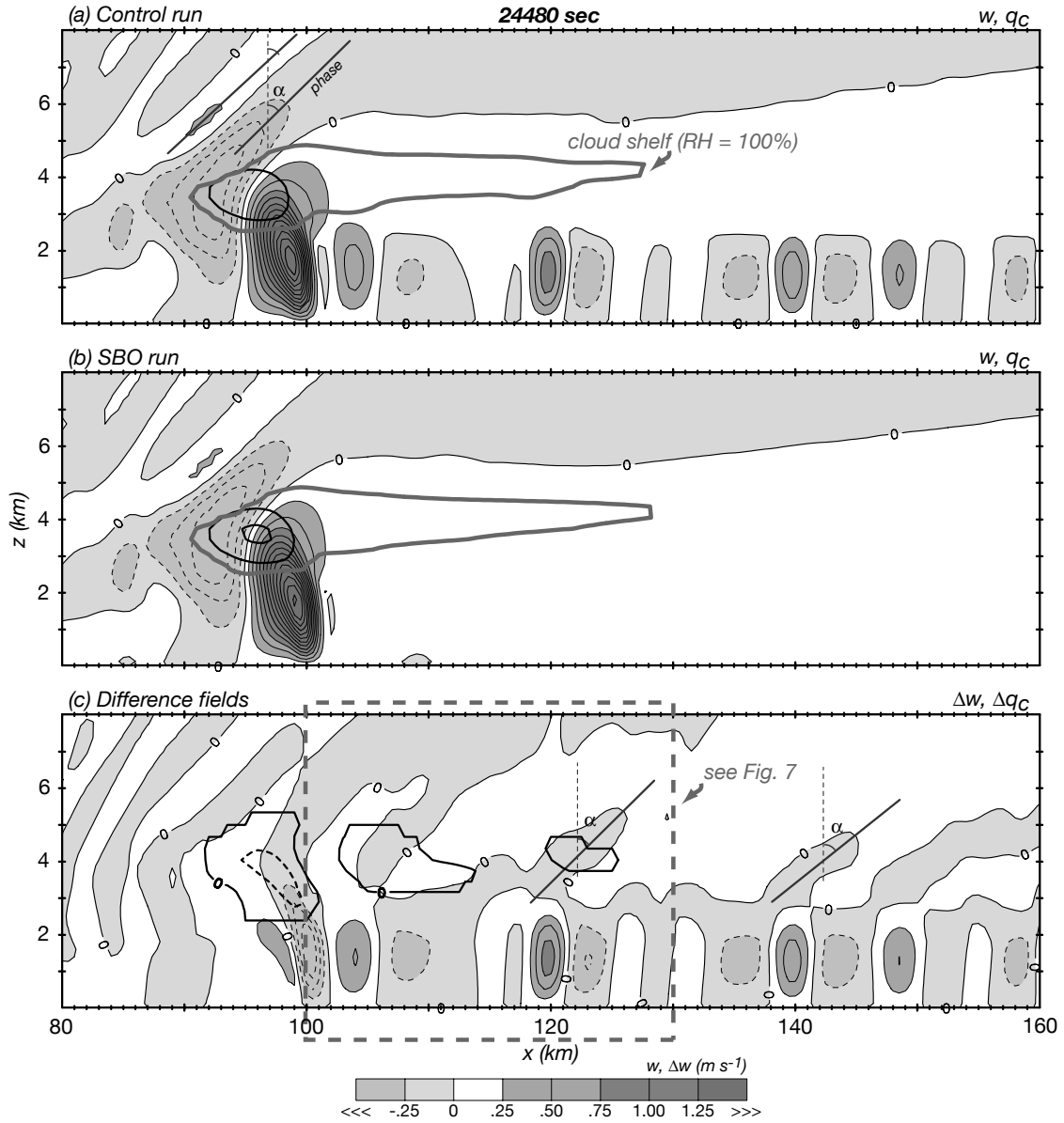
Fig. 5: Control, SBO and Control-SBO difference fields at 24480 sec. Panels (a) and (b) show vertical velocity w (shaded and contoured) and cloud water q_c (0.5 g kg^{-1} thick contours) with saturated region identified. Panel (c) depicts vertical velocity and cloud water difference fields Δw and Δq_c. Contour interval for Δq_c is 0.1 g kg^{-1}. Contours for negative values dashed. Figure 7's subdomain is delineated.
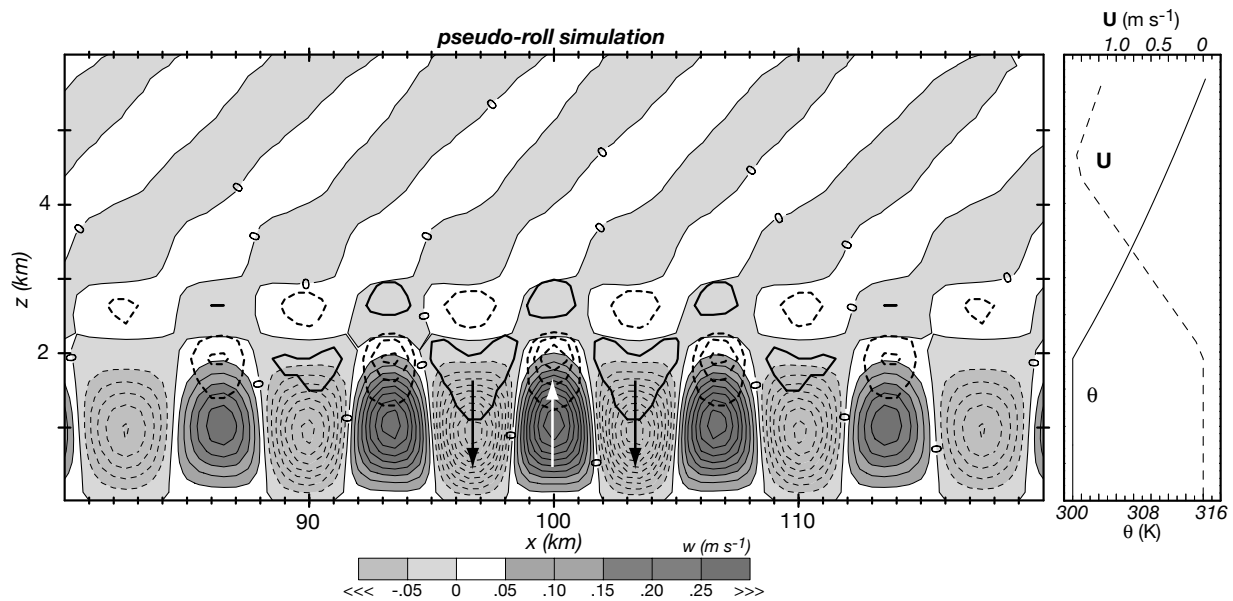
Fig. 6: Pseudo-roll simulation employing a maintained streamfunction field with weak forcing to generate roll-like circulations, showing vertical velocity w (shaded/contoured) and perturbation potential temperature θ' (0.005 K contours). Contours for negative values dashed. Profiles of u and θ at right resembles those present inland of the SBF in the early afternoon. (Vertical shear within the mixed layer has been neglected for simplicity.)

Fig. 7: Control-SBO difference fields at 24480 sec. Shown are: vertical velocity Δw (shaded), water vapor mixing ratio ($\Delta q_v'$, 0.1 g kg^{-1} thin black contours) and cloud water mixing ratio (δq_c, 0.01 g kg^{-1} thick grey contours) difference fields. Contours for negative values dashed. Saturated region from the SBO run is marked. Vertical profiles of u and w from the SBO run at a designated location reveals the background field upon which the Control run's rolls are superposed.
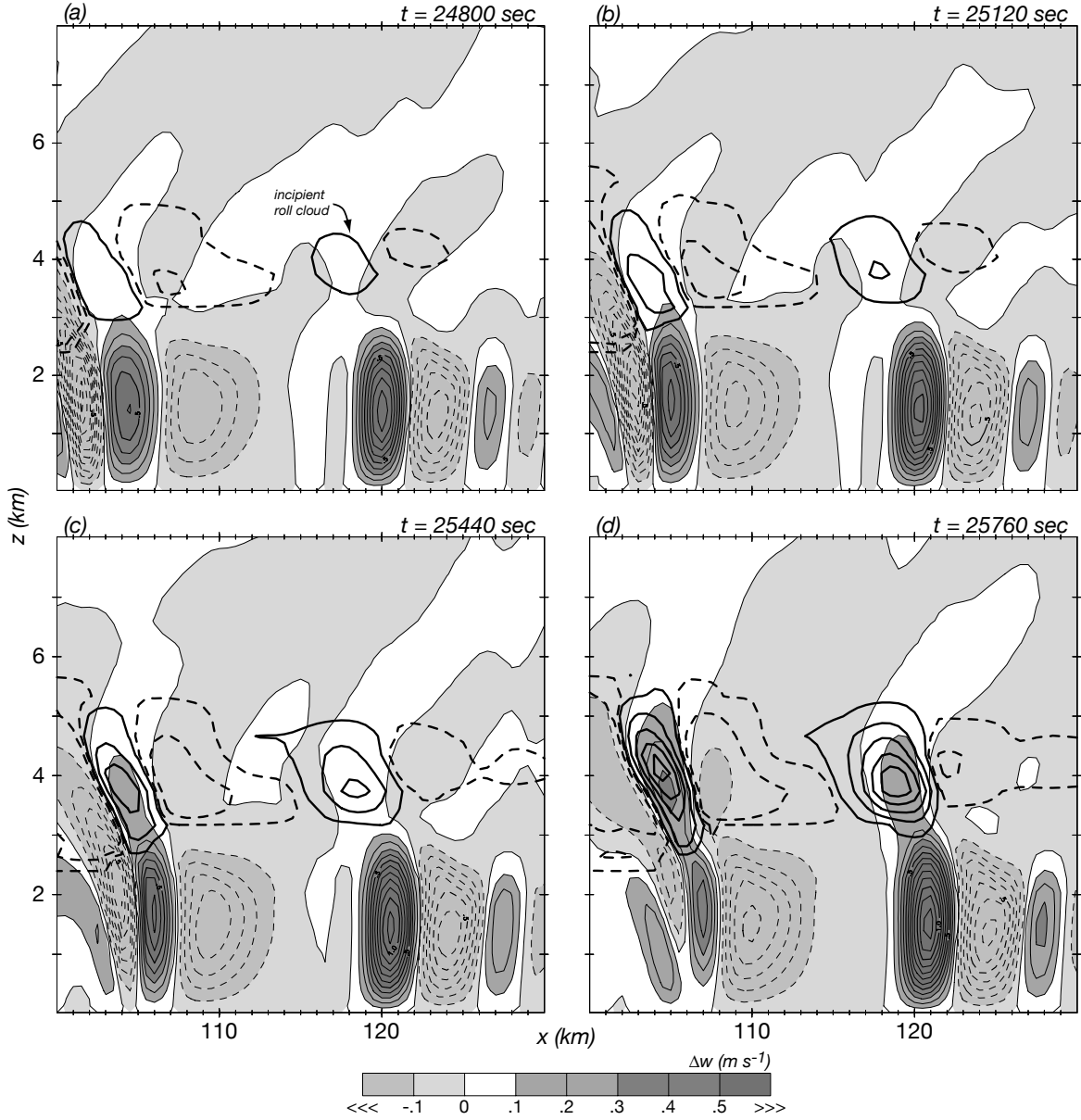
Fig. 8: Control-SBO vertical velocity (Δw, shaded/contoured) and cloud water (Δq_c) difference fields. Δq_c contours selected for inclusion are the 0.01, 0.05, 0.09, 0.13 and 0.17 g kg^{-1} isolines, in addition to the -0.0001 and -0.025 g kg^{-1} values. Contours for negative values dashed.
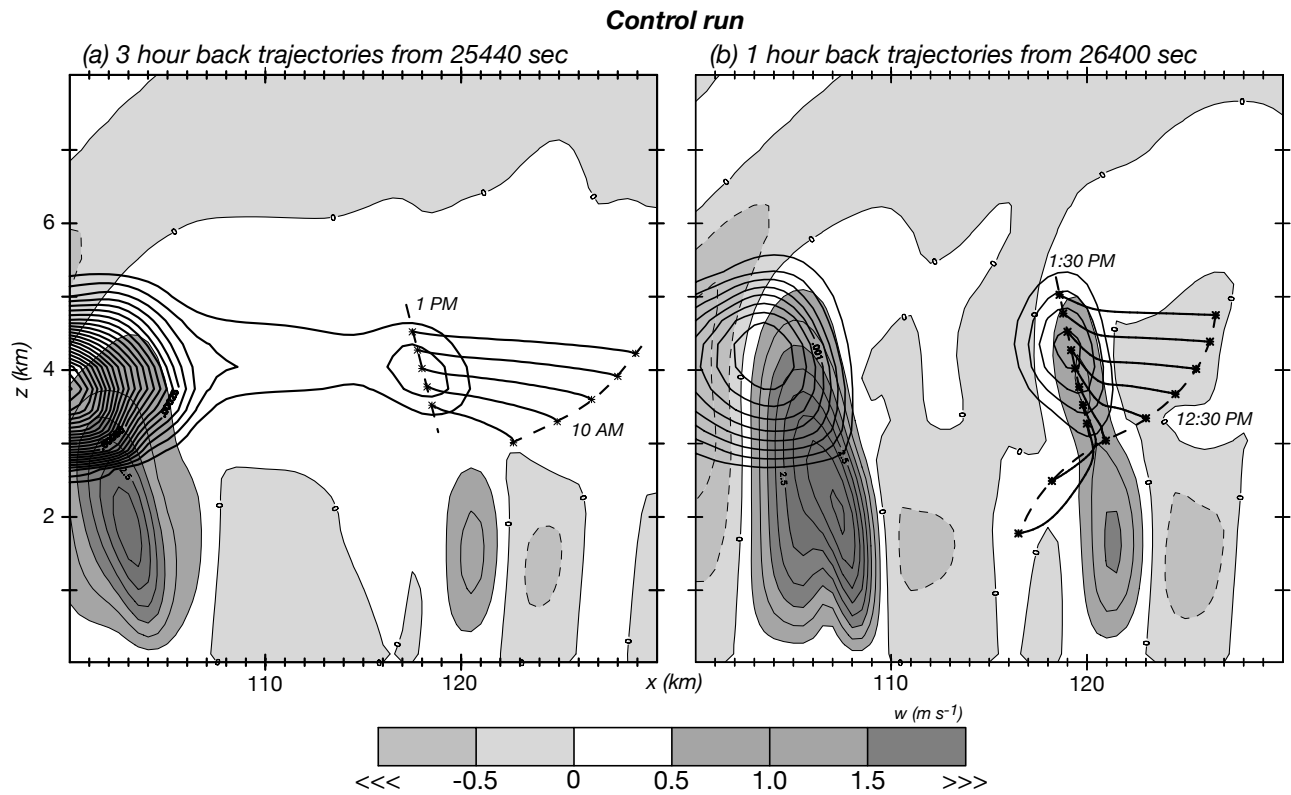
Fig. 9: Control run w (shaded/contoured) and q_c (contoured) fields with backward trajectories started at time shown: (a) fields at 25440 with q_c contour interval of 0.05 g kg^{-1}; (b) fields at 26400 sec with q_c contour interval 0.2 g kg^{-1}. Contours for negative values dashed. Please note cloud water contour intervals are not the same, and differ from that employed in Fig. 1.
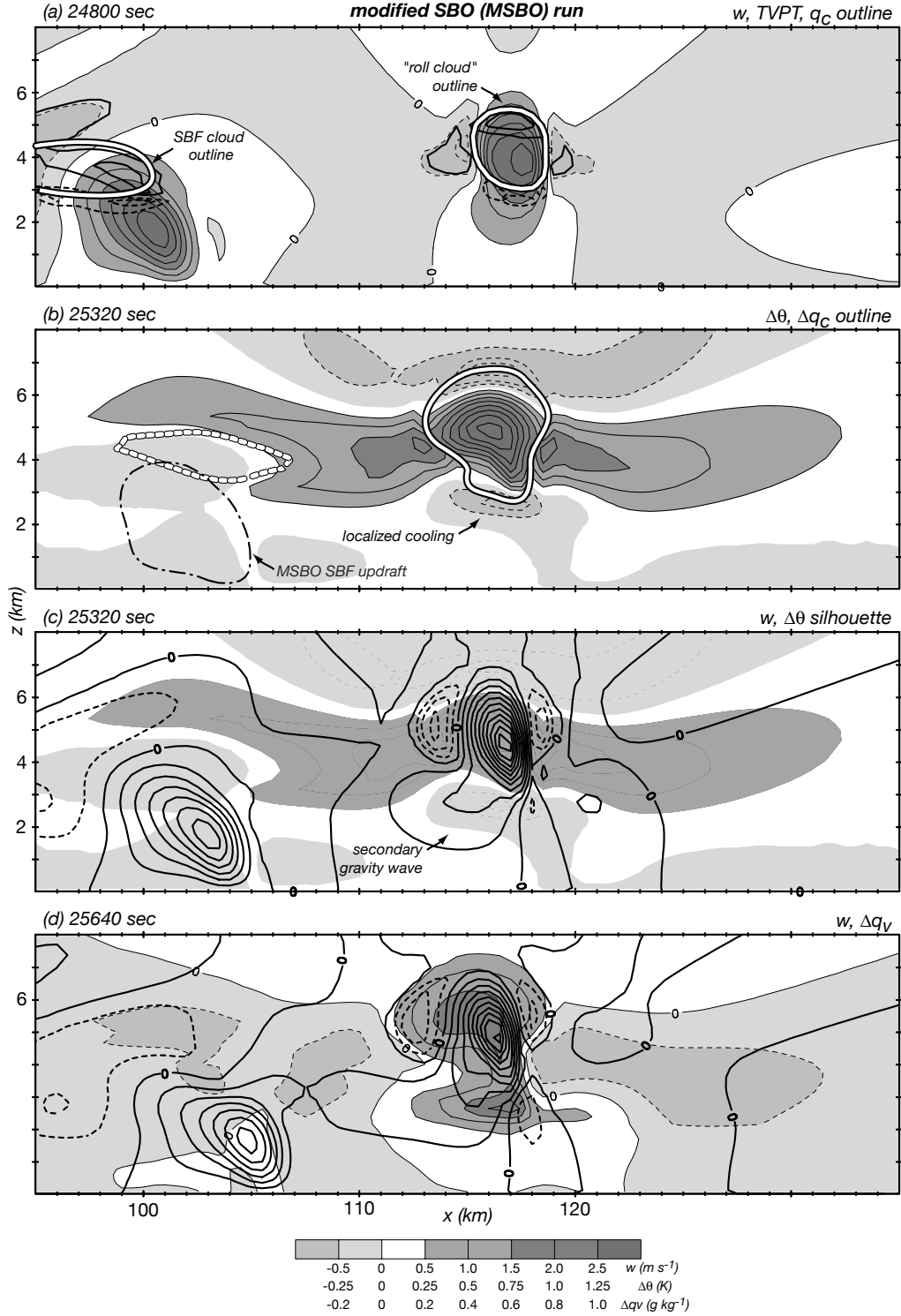
Fig. 10: Fields from the modified SBO (MSBO) run along with MSBO-SBO differences, depicting: (a) vertical velocity w (shaded/contoured), 0.5 g kg^{-1} cloud water outline (in white) and TVPT (0.02 K s^{-1} contours) at 24800 sec, 5 min after introduction of moisture perturbation in SBO run's cloud shelf; (b) MSBO-SBO potential temperature difference field ($\Delta\theta$, shaded/contoured) at 25320 sec with $\pm$ 0.15 g kg^{-1} cloud water (Δq_c,) difference contours (in white) superposed; (c) MSBO w field (0.5 m s^{-1} contours) at 25320 sec with $\Delta\theta$ silhouette for reference; and (d) w (0.5 m s^{-1} contours) and water vapor difference (Δq_v, shaded/contoured) fields at 25640 sec. Contours for negative values dashed. In (b), position of the MSBO SBF updraft shown by the 0.5 m s^{-1} w contour.
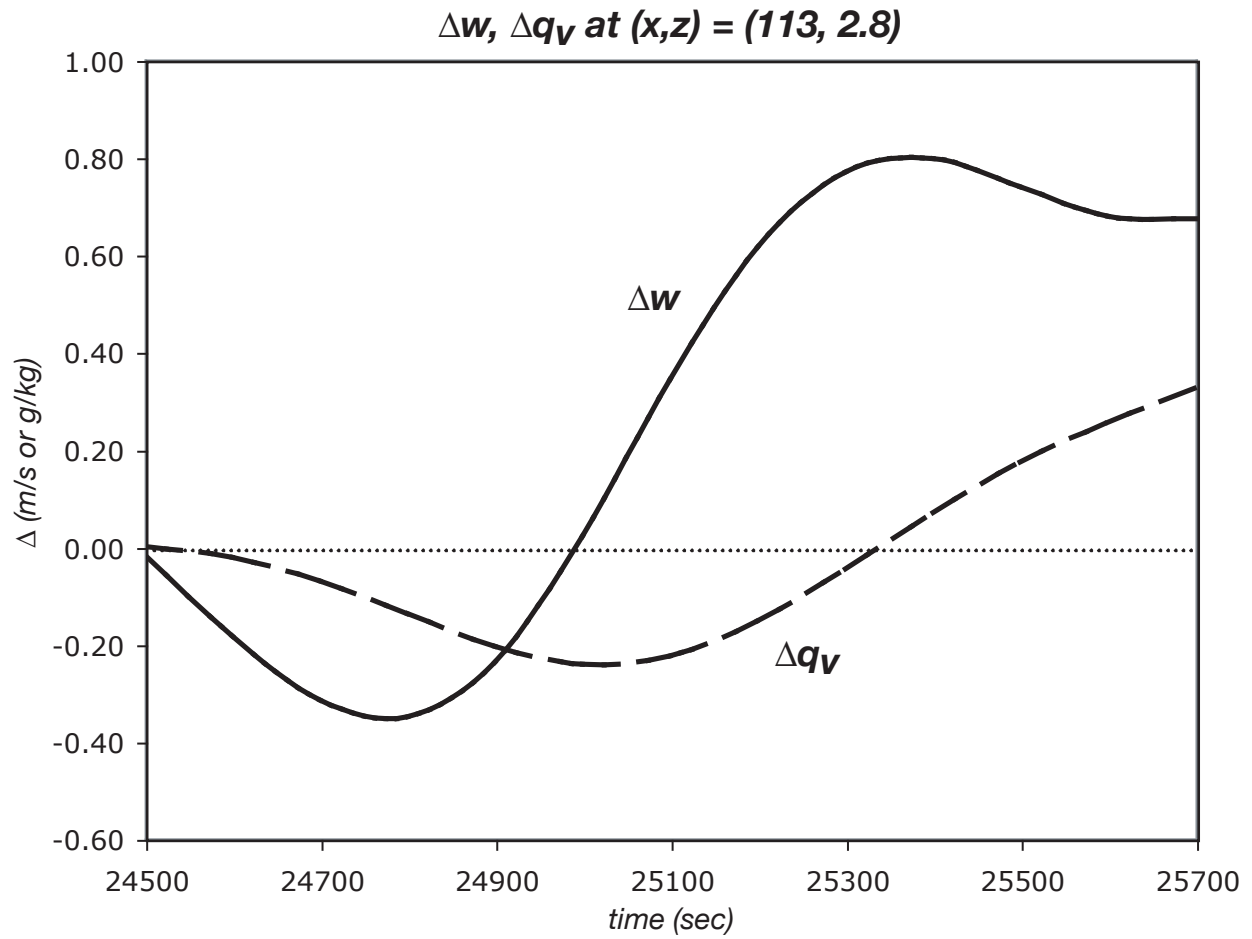
Fig. 11: Time series of MSBO-SBO vertical velocity and vapor mixing ratio difference fields, commencing at time of cloud shelf perturbation introduction in the latter, for the location $x = 113$ km and $z = 2.8$ km (refer to Fig. 10).
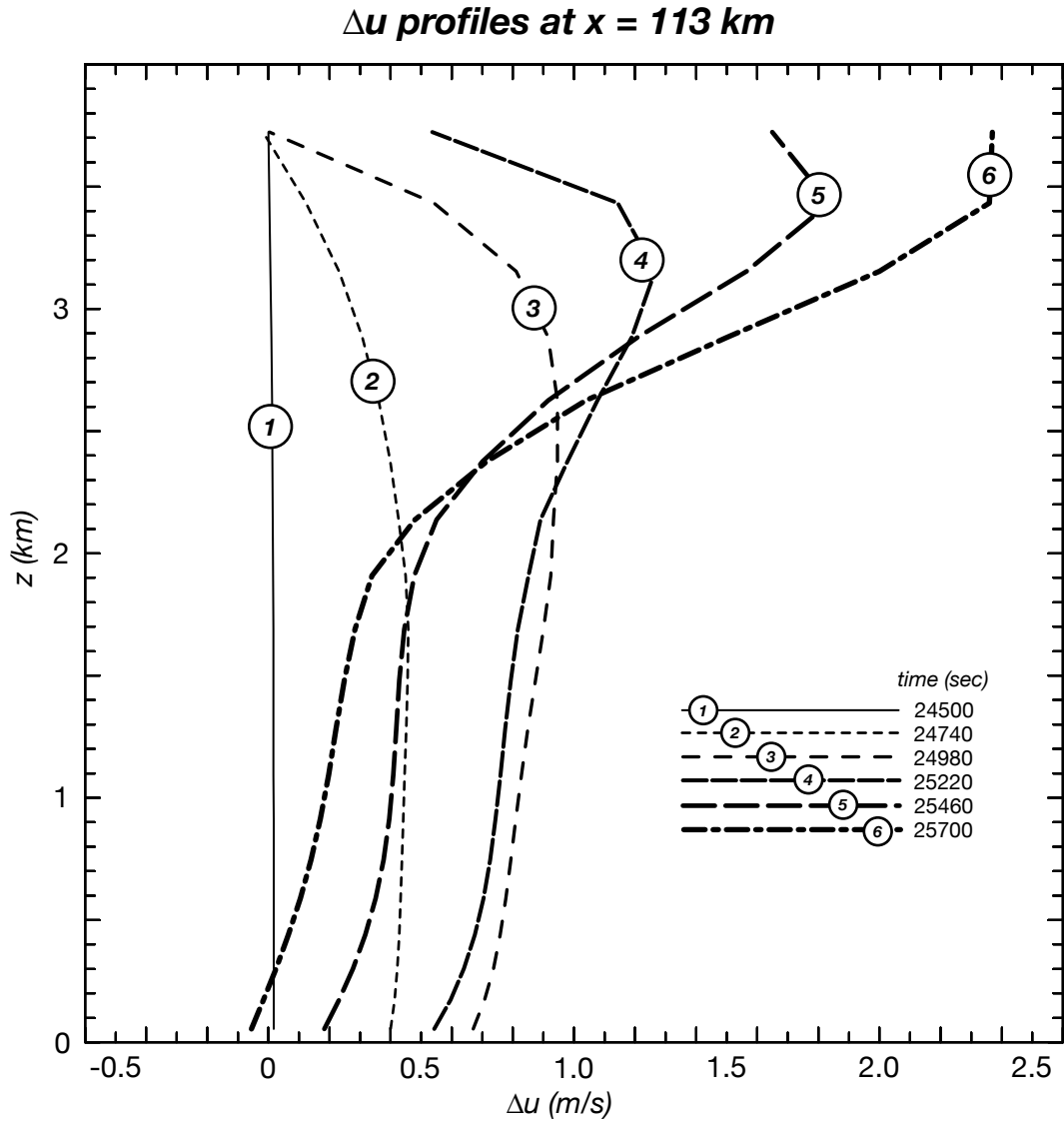
Fig. 12: Vertical profiles of MSBO-SBO horizontal velocity difference (Δu) at the location $x = 113$ km (refer to Fig. 10) for a variety of times following cloud shelf perturbation introduction.
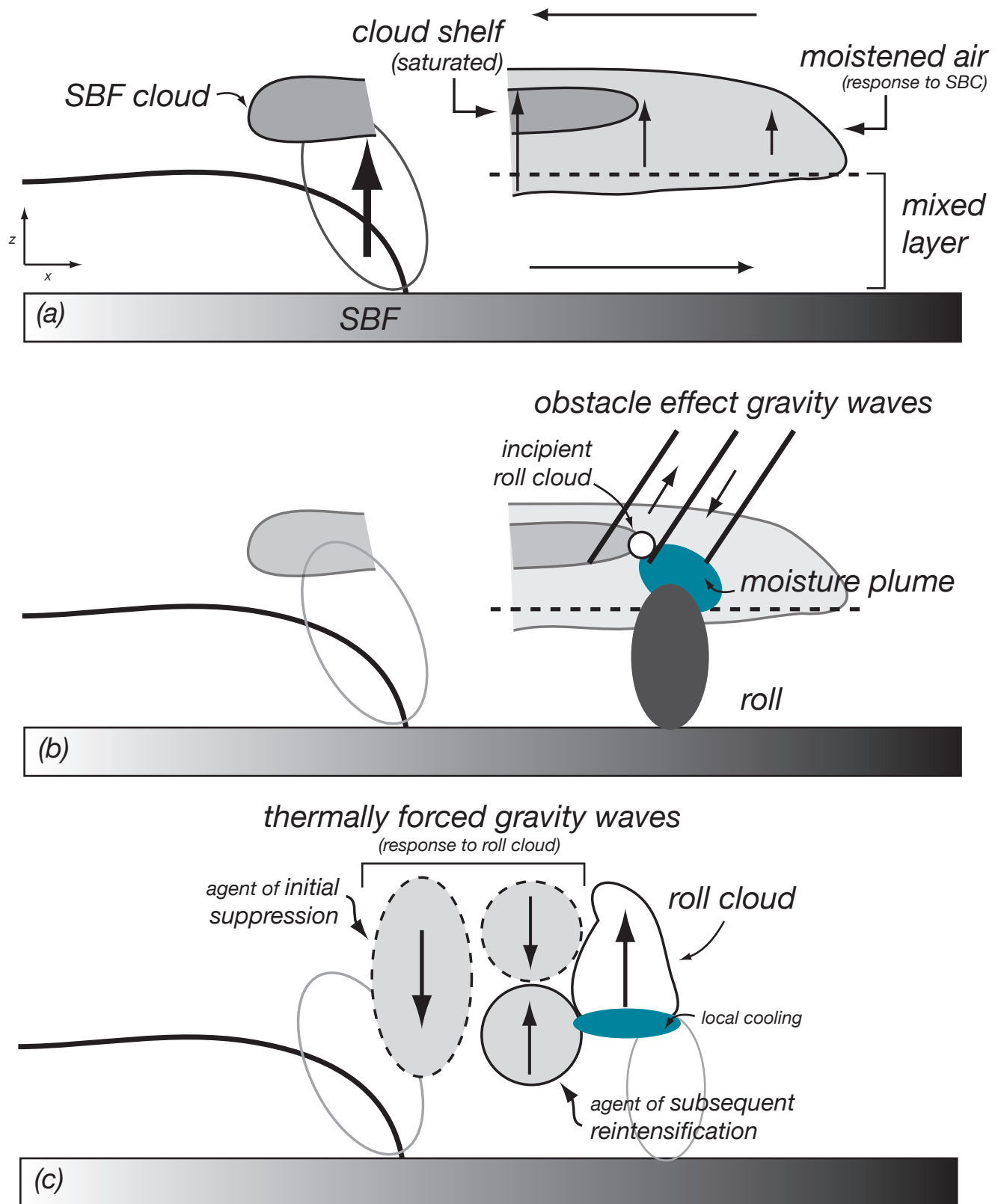
Fig. 13: Schematic depiction of SBC and roll-related influences leading to deep convection ahead of the SBF in the Control run. See text for discussion.